Phase Behavior and Ion Transport in Lithium−Niobium−Tantalum Oxide Alloys

Published as part of Chemistry of Materials special issue "Honoring the Outstanding Scientific Contributions of Clare Grey".

Hengning Chen, Zeyu Deng, Gopalakrishnan Sai Gautam, Yan Li, and Pieremanuele Canepa*

Cite This: https://doi.org/10.1021/acs.chemmater.5c02429

Read Online

ACCESS | Metrics & More | Article Recommendations | SI Supporting Information

ABSTRACT: Lithium niobate-tantalate mixtures have garnered considerable interest for their ability to merge the desirable properties of both end members, enabling diverse high-value applications, such as high-performance faradaic capacitors, non-linear optics, and protective coatings in rechargeable batteries. While numerous studies on the application of $LiNb_xTa_{1-x}O_3$ exist, the phase behavior and properties of $Li_3Nb_xTa_{1-x}O_4$ remain largely unexplored. In this work, we employ a multiscale approach that encompasses first-principles phonon calculations, cluster expansion, and Monte Carlo simulations to derive the temperature−composition phase diagram for $Li_3Nb_xTa_{1-x}O_4$. Our findings reveal the critical role of vibrational entropy in accurately predicting phase stability, which promotes the solubility of Nb in Li_3TaO_4 while suppressing the miscibility of Ta in Li_3NbO_4. Additionally, we demonstrate that Nb/Ta mixing offers a promising avenue for tailoring the Li-ion conductivities of $Li_3Nb_xTa_{1-x}O_4$. On the technical side, we demonstrated the importance of including vibrational entropy effects explicitly in Monte Carlo simulations dealing with multicomponent systems, beyond simple binary mixtures. On the application side, this study provides fundamental insights into the phase behavior and Li-ion transport properties of $Li_3Nb_xTa_{1-x}O_4$, paving the way for its potential applications in energy storage and other fields.
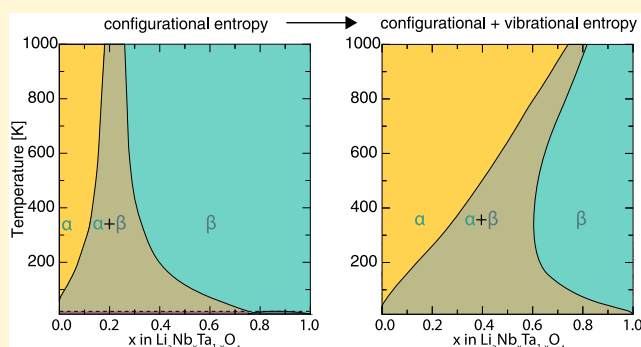
1. INTRODUCTION

Functional oxides are employed in a myriad of applications and technologically relevant devices.[1−3] These materials are often used as protective coating materials in energy storage and conversion applications.[4−7] In particular, the increasing demand for high-performance and safe energy storage devices has driven significant research into advanced lithium(Li)-ion batteries (LIBs) and all-solid-state batteries (ASSBs) with large gravimetric (volumetric) energy and power densities.[8,9] The improvement of the safety of these battery devices is not secondary. Unfortunately, LIB devices use flammable electrolytes and are plagued by a persistent cathode (positive electrode)-electrolyte interface degradation, hindering these cells' overall efficiencies and lifespans.[10,11] Li-metal anode-based ASSBs are claimed to offer safer and potentially higher energy and power densities compared to commercial LIBs, but face issues with electrode−electrolyte compatibility, inadequate physical contact between particles of solid electrolytes and the active materials, as well as metal ingress in the solid electrolyte separator.[8,12] Coating technologies have emerged as one of the most crucial strategies to mitigate some of these challenges in LIBs and ASSBs.[6,7,13,14] Functioning as physical

and chemical protective layers, coating materials can mitigate interface instabilities, modulate resistance to ion and electron transport, and improve the overall cell performance.[4,15,16]

Prior experimental works have demonstrated the great potential of both amorphous and crystalline Li−Nb−O and Li−Ta−O coatings for positive electrode materials in LIBs and ASSBs.[17−20] Several authors have speculatively claimed that amorphous $LiNbO_3$ and $LiTaO_3$ materials exhibit adequate ionic conductivities ($\sim10^{-6} - 10^{-7}$ S cm^{-1}) at room temperature, which might be attributed to their high porosity (approximately 22% free volume).[21−23] Crystalline niobate and tantalate coatings reveal a complex multiphasic nature comprising $LiMO_3$ and Li_3MO_4 (M = Nb, Ta) phases,[18,24−26] with Li_3MO_4 actively involved in Li-ion transport due to its defect-rich landscape.[24,27,28]

A
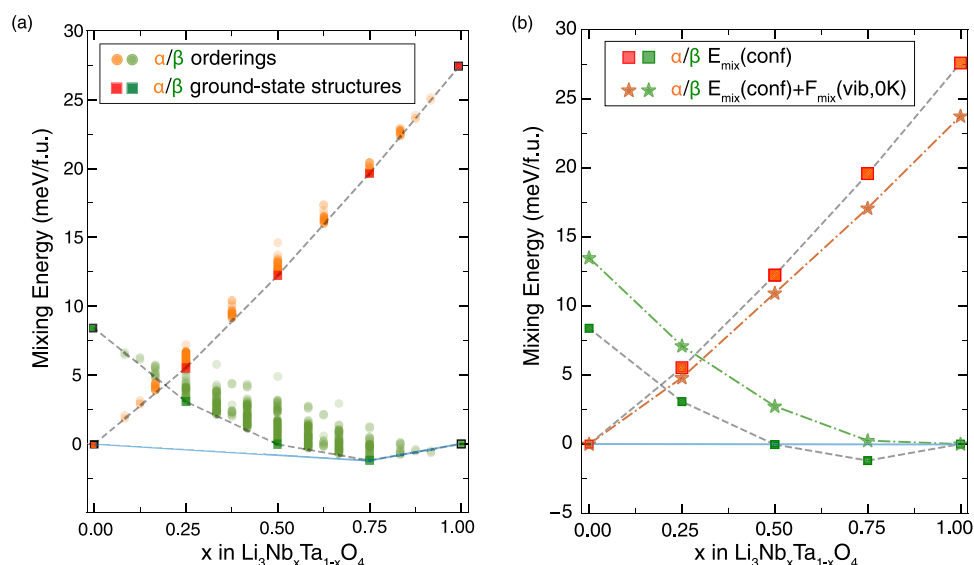
Figure 1. Combined mixing energies of α-phase and β-phase $Li_3Nb_xTa_{1-x}O_4$ systems: (a) Configurational mixing energies of all Nb/Ta ordering models explored, (b) Configurational and vibrational mixing energies (at 0 K) of only ground-state structures based on DFT calculations. The α- and β-phase substituted configurations are displayed with orange and green filled points. Blue solid lines in (a) and (b) represent the global convex hull, while dashed lines show the convex hull envelopes constructed by the ground-state structures of α and β phases, separately. In the α-phase, the ground-state structures (red squares) are $Li_3TaO_4(C2/c)$, $Li_3Ta_{0.75}Nb_{0.25}O_4(P1)$, $Li_3Ta_{0.5}Nb_{0.5}O_4$ (Cc), $Li_3Ta_{0.25}Nb_{0.75}O_4(P1)$, $Li_3NbO_4(C2/c)$. In β-phase, the ground-state structures (green squares) are $Li_3TaO_4(I\overline{4}3m)$, $Li_3Ta_{0.75}Nb_{0.25}O_4(R3m)$, $Li_3Ta_{0.5}Nb_{0.5}O_4$ $(Fmm2)$, $Li_3Ta_{0.25}Nb_{0.75}O_4(R3m)$, $Li_3NbO_4(I\overline{4}3m)$.

In 2015, utilizing physical vapor deposition approach, Yada et al. conducted a high-throughput exploration of the phase-space of the $LiNb_xTa_{1-x}O_3$ system.[29] They reported enhanced Li-ion conductivity in the partially crystallized $Li_{56}Nb_{22}Ta_{22}$ oxide (4.2×10^{-6} S cm^{-1}) and higher permittivity of $\sim$165 (when measured at 254 kHz) compared to pure $LiNbO_3$ (1.8×10^{-6} S cm^{-1} and a permittivity of $\sim$95, respectively). Generally, $LiNb_xTa_{1-x}O_3$ demonstrates improved Li-ion diffusion and reduced charge transfer resistance at interfaces within ASSBs.[30,31] As the concentration of Nb (x) increases, the ionic conductivities of $LiNb_xTa_{1-x}O_3$ first increase and then decline, culminating in peak conductivity when $x = 0.5$. This finding is further supported by Wang et al.,[32] wherein the ionic conductivity of partially crystallized $LiNb_{0.5}Ta_{0.5}O_3$ reaches 38.7×10^{-6} S cm^{-1}.

Due to the isovalent electronic configuration and nearly identical ionic radii (64 pm) of Nb^{5+} and Ta^{5+} when six-coordinated,[33] tantalum can easily substitute on Nb sites without introducing intrinsic defects, such as vacancies or interstitials. Mixing $LiNbO_3$ with $LiTaO_3$ phases exhibits complete solid solubility across the entire composition range.[34,35]

Despite the extensive research on the $LiNb_xTa_{1-x}O_3$ system,[36−39] understanding the phase behavior of $Li_3Nb_xTa_{1-x}O_4$ is crucial for designing superior crystalline coating materials, which remains unexplored. Indeed, the chemical and structural similarities of "pentavalent" Nb and Ta do not directly translate to the observed properties of the niobate and tantalate mixture, necessitating further research. To bridge this knowledge gap, this study examines the phase stability of $Li_3Nb_xTa_{1-x}O_4$ by providing a complete thermodynamic picture of this system that incorporates both configurational and vibrational entropy contributions. Since the cubic Li_3NbO_4 ($I\overline{4}3m$) and monoclinic Li_3TaO_4 ($C2/c$) phases are not isostructural, their mixing will give rise to heterostructures.[40−42] Therefore, we define the α tie line as the

substitution of Ta with Nb in the monoclinic Li_3TaO_4 structure, and the β tie line as the substitution of Nb with Ta in the cubic Li_3NbO_4 structure.

Employing a multiscale approach parametrized on accurate first-principles calculations, cluster expansion methods, phonon calculations, and atomistic Monte Carlo (MC) simulations, we investigate the mixing of Nb and Ta in the pseudobinary $Li_3Nb_xTa_{1-x}O_4$ system. Our findings reveal the significant contribution of lattice vibrations to the phase transition in $Li_3Nb_xTa_{1-x}O_4$, resolving discrepancies between theoretical predictions, considering, at best, only configurational entropy and experimental observations. This discrepancy can be attributed to the distinct vibrational characteristics of Nb−O and Ta−O bonds and differences in atomic arrangements inherent to the Li_3NbO_4 and Li_3TaO_4 local structures. We observe that the Li-ion conductivity of $Li_3Nb_xTa_{1-x}O_4$ increases with the degree of cation mixing within both α- and β-phases. This work provides a comprehensive understanding of the phase behavior and conduction properties of $Li_3Nb_xTa_{1-x}O_4$, paving the way for the design of advanced coating materials for energy storage and conversion applications.

2. METHODS

2.1. First-Principles Calculations. We conducted density functional theory (DFT) calculations as implemented in the Vienna *ab initio* Simulation Package (VASP).[43] In DFT, the unknown exchange-correlation energy was approximated by the meta-GGA functional r^{2}SCAN.[44] To systematically explore a diverse range of Nb/Ta mixing configurations in $Li_3Nb_xTa_{1-x}O_4$, we generated all possible orderings in supercell models, accommodating up to 16 formula units (128 atoms) for the cubic phase of Li_3NbO_4 and the monoclinic phase of Li_3TaO_4. At each composition in the $Li_3Nb_xTa_{1-x}O_4$ tie-line, a maximum of 1,000 distinct Nb−Ta orderings with the lowest Ewald energy were initially stored,[45,46] followed by the selection of only symmetrically inequivalent structures. The computational methodology for relaxing the

$Li_3Nb_xTa_{1-x}O_4$ orderings follow the procedures in our previous study.[24] Specific parameters, such as wave function energy cutoff, the projector augmented wave potentials, and details of the total energy integration in the first Brillouin zone, are provided in the SI.

2.2. Cluster Expansion. We applied the cluster-expansion (CE) formalism to the Nb and Ta distributions in the $Li_3Nb_xTa_{1-x}O_4$ system. Based on the approach introduced by Sanchez et al.,[47] the CE model connects the effective cluster interactions, V_α, in eq 1 with the configurational mixing energies (E_{mix}(conf) of eq 2) of distinct Nb/Ta orderings calculated by DFT on supercell models of finite size. The fitting of the CE was performed using the cluster-assisted statistical mechanics (CASM) package,[48−50] where E_{mix}(conf) depends on an expansion of different cluster functions (eq 1)

$$E_{mix}(conf) = \sum_\sigma \sum_\alpha V_\alpha \overline{\prod_\alpha(\vec{\sigma})}; \; \vec{\sigma} = (\sigma_1, \sigma_2, \cdots, \sigma_i) \quad (1)$$

where $\vec{\sigma}$ are configuration vectors, consisting of occupation variables, $\sigma_i = -1$ or 1, representing the Nb or Ta occupancies of specific crystallographic sites, i. V_α refers to the effective cluster interactions (ECIs), including the multiplicity of symmetrically equivalent clusters, α. In the $Li_3Nb_xTa_{1-x}O_4$ systems, pairs, triplets, and quadruplets cluster interactions are truncated at maximum radii of 12 Å, 7 Å, and 5 Å, respectively. To increase the sparsity of the ECI solutions, we applied the compressive sensing algorithm to determine the optimal set of ECIs. Here, we employed the hyperparameter $\alpha = 1 \times 10^{-6}$ to solve the least absolute shrinkage and selection operator problem.[51]

To construct the phase diagram for $Li_3Nb_xTa_{1-x}O_4$, we combined the results from both substitution systems, using the stable phases as reference end points, α-Li_3TaO_4 and β-Li_3NbO_4 in the pseudobinary tie line, as depicted in Figure 1. Thus, the configurational mixing energy E_{mix}(conf) is calculated as in eq 2

$$E_{mix}(conf) = E(Li_3Nb_xTa_{1-x}O_4) - (1 - x)E(\alpha - Li_3TaO_4)$$
$$- xE(\beta - Li_3NbO_4) \quad (2)$$

where $E(Li_3Nb_xTa_{1-x}O_4)$, $E(\alpha$-$Li_3TaO_4)$, and $E(\beta$-$Li_3NbO_4)$ are the DFT total energies of each Nb/Ta ordering and the two stable end-member structures at 0 K.

2.3. Vibrational Entropy Contributions in $Li_3Nb_xTa_{1-x}O_4$. From two $Li_3Nb_xTa_{1-x}O_4$ substitution systems, i.e., the α-phase and the β-phase, 10 ground-state structures at selected compositions $x = 0$, 0.25, 0.5, 0.75, and 1 were chosen for harmonic phonon calculations obtained with Phonopy and VASP.[52] In these calculations (on 32-atom large cells), stricter convergence criteria were imposed to accept structure convergence: 10^{-8} eV for the DFT total energy and 10^{-3} eV/Å for the Hellmann−Feynman forces. Starting from 32-atom cells of stable $Li_3Nb_xTa_{1-x}O_4$ compositions, $2 \times 2 \times 2$ supercells (256 atoms) were generated for finite difference calculations. Brillouin-zone paths in the phonon band structure plots were obtained with SeeK-path by Hinuma et al.[53] Phonon band structures and phonon density of states are plotted in the SI (Figures S13−S14).

The mixing vibrational free energy,[54] F_{mix}(vib), captures the compositional (x) and temperature (T) dependence relative to the vibrational free energies of the two stable end members, α-Li_3TaO_4 and β-Li_3NbO_4.

$$F_{mix}(vib, T) = F_{vib}(Li_3Nb_xTa_{1-x}O_4, T) - xF_{vib}(\beta - Li_3NbO_4, T)$$
$$- (1 - x)F_{vib}(\alpha - Li_3TaO_4, T) \quad (3)$$

where $F_{vib}(Li_3Nb_xTa_{1-x}O_4,T)$, $F_{vib}(\beta$-$Li_3NbO_4,T)$, and $F_{vib}(\alpha$-$Li_3TaO_4,T)$ are the vibrational free energies of $Li_3Nb_xTa_{1-x}O_4$, β-phase Li_3NbO_4, and α-phase Li_3TaO_4 at specific temperature, T, respectively. At each temperature, we used a cubic-type polynomial form to interpolate values of F_{mix}(vib) at intermediate compositions, which are then incorporated in the Monte Carlo simulations.

2.4. Monte Carlo Simulations. To include effects of vibrational free energy, estimated values of F_{mix}(vib, x, T) at specific compositions and temperatures are passed to the Monte Carlo routines in a modified version of the CASM code,[55] where we incorporated directly dF_{mix}(vib) −the derivatives of the vibrational free energies of mixing− into the Metropolis step.

For substitution in both α- and β-phases, we carried out semigrand canonical MC simulations based on $10 \times 10 \times 10$ model supercells (with 4,000 f.u.) by performing separate chemical potential (μ) and temperature (T) MC scans.[56] First, the scan started from T = 10 K and up to T = 1,000 K with a step of $\Delta T = 10$ K in the range of $\mu = [-1.0, 1.0]$ eV/f.u. ($\Delta\mu = 0.01$). Then at every temperature value, μ was scanned in both the forward (Li_3TaO_4, $x = 0 \rightarrow Li_3NbO_4$, $x = 1$, i.e., from $\mu = -1.0$ to $+1.0$ eV/f.u.) and the backward ($x = 1 \rightarrow x = 0$, from $\mu = +1.0$ to -1.0 eV/f.u.) directions with a step size $\delta\mu = \pm 0.01$ eV/f.u. With these settings, we explored two distinct phase diagrams, one for the α phase and the other for the β phase. The complete phase diagram was obtained by comparing the semigrand canonical potentials of the two phases across the entire composition range to identify the stable structure. Details of the integration methods are described in the SI.

2.5. Li^+ Mobility with Machine Learning Molecular Dynamics. We started from $Li_3Nb_xTa_{1-x}O_4$ configurations ($2 \times 2 \times 2$ supercells, 32 f.u.) obtained with semigrand canonical Monte Carlo simulations of representative compositions at 300 K. After DFT geometry optimizations of these structures (see details in Section 2.1), we performed AIMD simulations within the low-limit vacancy regime (one Li vacancy, Vac_{Li}, in $Li_{95}Ta_{32(1-x)}Nb_{32x}O_{128}$) to generate the training sets for fitting the machine learning potential. The plane-wave energy cutoff was set to 400 eV, and employed the Nosé-Hoover thermostat. The Newton equation of motion was integrated with a time step of 0.5 fs. AIMD simulations were executed for all configurations at 600, 800, 1,000, and 1,200 K for 10 ps, incorporating an initial temperature ramping of 0.5 ps.

The moment tensor potentials (MTP) are individually trained for each Ta/Nb concentration using 32,000 AIMD snapshots, specifically the final 4 ps trajectory of each temperature. During the MTP training, we set the hyperparameter lev_{max} of 12 and R_{cut} to be 7 Å to ensure robust fitting and validation accuracies in energies, forces, and stresses. Extended MD trajectories (10 ns) were obtained after a temperature ramping of 10 ps (to reach the target temperature) and a following period of equilibration of 1 ns.

3. RESULTS

3.1. Phase Stabilities of $Li_3Nb_xTa_{1-x}O_4$. Li_3NbO_4 and Li_3TaO_4 crystallize in distinct structure archetypes. The cubic Li_3NbO_4 (space group: $I\bar{4}3m$) features Nb sites (8c) forming edge-sharing Nb octahedra arranged in Nb_4O_{16} clusters (Figure S4a). The monoclinic Li_3TaO_4 (space group: $C2/c$) shows distinct edge-sharing Ta octahedra giving rise to zigzag chains along the c direction (Figure S4b). Because Li_3NbO_4 and Li_3TaO_4 are not isostructural, their $Li_3Nb_xTa_{1-x}O_4$ alloys will form a heterostructure resulting from the combination of cubic and monoclinic crystal systems.[40−42] To understand the formation of heterostructures, we initially study the isostructural alloying process denoting the substitution of Ta with Nb in the monoclinic Li_3TaO_4 structure as the α tie line, and the substitution of Nb with Ta in the cubic Li_3NbO_4 structure as the β tie line. Subsequently, by implementing convex hull minimization (as a function of varying Nb content), we combine these isostructural tie lines to investigate the formation of possible heterostructures.

The mixing energies of $Li_3Nb_xTa_{1-x}O_4$ α- and β-phase orderings were calculated as a function of composition (x) (Figure 1a). In the β-phase substitution, the resulting β-Li_3TaO_4 (green square at $x = 0$) maintains the cubic $I\bar{4}3m$ structure of the β-Li_3NbO_4 (green square at $x = 1$). All β-phase configurations feature $(Nb/Ta)_4O_{16}$ clusters with a close resemblance to the β-Li_3NbO_4 structure. Similarly, in the α-phase substitution, both α-Li_3TaO_4 (red square at $x = 0$) and α-Li_3NbO_4 (red square at $x = 1$) retain the monoclinic $C2/c$
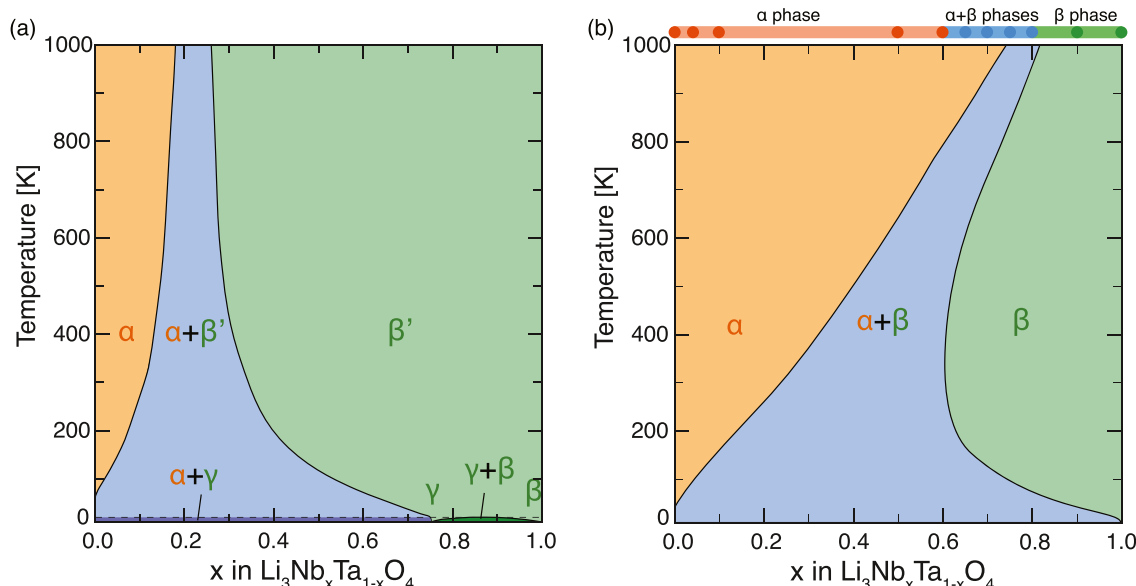
Figure 2. Computed phase diagrams of $Li_3Nb_xTa_{1-x}O_4$ from semigrand canonical MC simulations at different temperatures (vertical axis) vs variable compositions (horizontal axis), including (a) configurational entropy, (b) configurational and vibrational entropy effects. Colored dots on the top x-axis of (b) show the sequence of stable $Li_3Nb_xTa_{1-x}O_4$ phases experimentally synthesized at 1273 K.[64]

structure. All α-phase mixed configurations exhibit zigzag chains of Nb/Ta octahedra as in Li_3TaO_4, although usually with lower symmetry.

From the convex hull in Figure 1a, it is clear that the polymorphs generated from substitutions, i.e., α-Li_3NbO_4 and β-Li_3TaO_4 are metastable. These results confirm the greater stability of β-Li_3NbO_4 and α-Li_3TaO_4, consistent with experimental observations.[57,58] The global convex hull comprises α-Li_3TaO_4, β-$Li_3Ta_{0.25}Nb_{0.75}O_4$, and β-Li_3NbO_4. The slightly negative mixing energy (-1.2 meV/f.u.) of $Li_3Ta_{0.25}Nb_{0.75}O_4$ suggests a weak thermodynamic driving force for Nb/Ta mixing. Other Nb/Ta mixing configurations (green and orange points in Figure 1) are metastable and prone to proportional decompositions —that is phase separation— into nearby stable phases.

To investigate the temperature and composition-dependent thermodynamic properties of $Li_3Nb_xTa_{1-x}O_4$, we employed DFT calculations of many Nb/Ta orderings (see Section 2.2) to parametrize a cluster expansion (CE) Hamiltonian. Subsequently, the CE Hamiltonian was used to perform semigrand canonical Monte Carlo simulations probing the effect of temperature on the mixing properties of the $Li_3Nb_xTa_{1-x}O_4$ system.

Of the DFT-calculated configurations, 221 and 489 for α-phase and β-phase orderings, respectively, are selected for fitting the CE model (Figure S4a,b). The effective cluster interactions (ECIs) were determined by minimizing the root-mean-square error (RMSE) between the CE model predictions and all DFT-calculated energies. The leave-one-out cross-validation (LOOCV) score was used to evaluate the predictive accuracy of the CE. The final ECIs for the α- and β-phases in Figures S5 and S6 are obtained with small values of RMSEs $\sim$0.30, 0.33 meV/f.u., and LOOCV scores $\sim$0.36, 0.50 meV/f.u., respectively. As illustrated in Figures S5 and S6, the cluster expansion analysis reveals that the nearest-neighbor pair interactions between Nb and Ta substitutions dominate the mixing energy landscape, with higher-order triplet and quadruplet clusters contributing negligibly.

Given the proximity in configurational mixing energies (within 30 meV/f.u.) among the phases defining the 0 K convex hull, the calculated mixing vibrational free energy contributions ($-20 \sim 25$ meV/f.u. in the 0–1,000 K range) are likely to influence the relative stability of ground-state structures. As shown in Figure S10, the vibrational free energies exhibit a near-linear relationship as a function of concentration x, which follows Vegard's law (except for some minor deviations). This behaviour allow us to implement a smooth interpolation of the ground state values at each temperature (Figure S11), thereby efficiently determining the vibrational free energies of $Li_3Nb_xTa_{1-x}O_4$ at other concentrations, thus bypassing computationally demanding calculations for all configurations[59] or more complex uses of the CE paradigm.[60−63] The implementation of an interpolation scheme following a Vegard-type behavior is further justified by a linear increase of unit cell volumes as the concentration of Nb increases in $Li_3Nb_xTa_{1-x}O_4$ (Figure S9 in SI).

The values of $F_{mix}(vib)$ were then added to $E_{mix}(conf)$ in Figure 1b (at 0 K) and incorporated with the subsequent MC simulations at all temperatures (Figure 2b accompanied by a detailed description in SI) considered. As shown in Figure S11, $F_{mix}(vib)$ exhibits negative values in α-phase substitution but positive values in β-phase substitution. This result suggests that the thermal vibrations stabilize the α-phase ($C2/c$ Li_3TaO_4) substitution while destabilizing the β-phase ($I\bar{4}3m$ Li_3NbO_4) substitution. The total mixing energy, i.e., configurational energy, $E_{mix}(conf)$ and vibrational free energy, $F_{mix}(vib)$, at $Li_3Ta_{0.25}Nb_{0.75}O_4$ consequently increases to 0.25 meV/f.u., leading to the disappearance of this global minima ($x = 0.75$).

Based on the DFT-calculated orderings and CE Hamiltonian, the temperature vs Nb composition (x in $Li_3Nb_xTa_{1-x}O_4$) phase diagram was constructed by minimizing the free energies of the α-phase and the β-phase substitutions from semigrand canonical MC simulations. Figure 2a depicts the phase diagram of $Li_3Nb_xTa_{1-x}O_4$ by only considering the configurational entropy of both systems (eq 4). In contrast, Figure 2b includes both configurational and vibrational
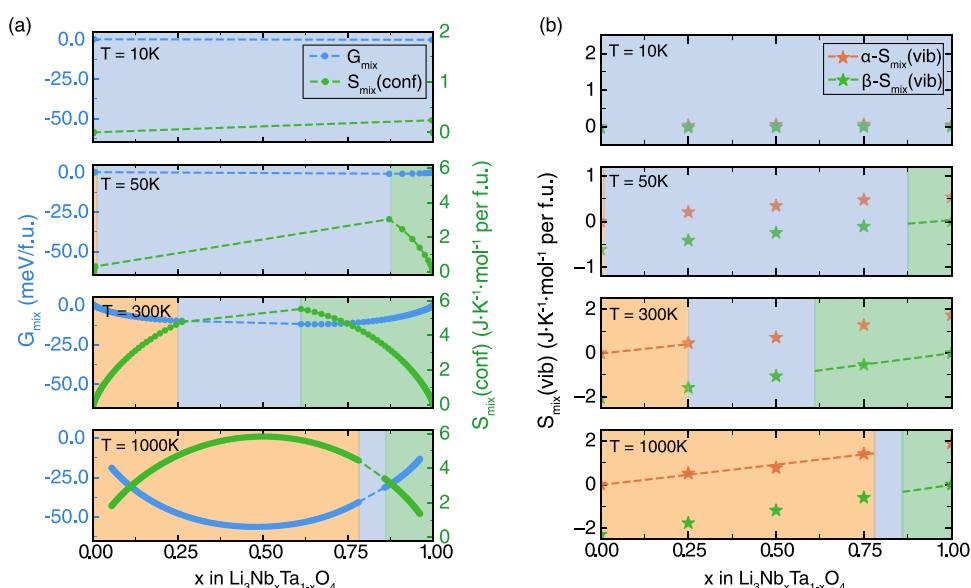
Figure 3. Thermodynamic properties (vertical axis) are shown as a function of Nb composition (x, horizontal axis). (a) Gibbs free energy G_{mix} (blue), configurational entropy of mixing $S_{mix}(conf)$ (green), and (b) Vibrational entropy of mixing $S_{mix}(vib)$ is plotted against composition (x) for the α (orange) and β (green) phases at 10, 50, 300, and 1,000 K. Stars denote the $S_{mix}(vib)$ values calculated for the ground-state structures at these temperatures. The colored regions indicate the phase distributions of α-phase (orange), $\alpha + \beta$ biphasic region (blue), β-phase (green) at corresponding temperatures.

entropies into the MC simulations (eq 5). Section 2.4 and SI describe in detail the computational approach.

$$\Phi_{MC}(conf) = E_{mix}(conf) - TS_{mix}(conf) - \mu x \quad (4)$$

$$\Phi_{MC}(conf, vib) = \Phi_{MC}(conf) + \underbrace{E_{mix}(vib) - TS(vib)}_{F_{mix}(vib)} \quad (5)$$

As shown in Figure 2a, α phase include configurations generated through the α-phase substitution, while γ, β, β' phases are based on β-phase structure type. All these single phases are separated by various biphasic regions. γ phase, which maintains the $R3m$ space group of $Li_3Ta_{0.25}Nb_{0.75}O_4$ and is characterized by the Nb_3TaO_{16} clusters, can only exist at very low temperatures (<30 K). The biphasic $\gamma + \beta$ (dark green) domain ceases above ~30 K, forming a wide single-phase region ($0.26 < x < 1$ at 1,000 K) of $Li_3Nb_xTa_{1-x}O_4$, β'. The dashed black lines differentiate $\alpha + \gamma$ (purple) and $\alpha + \beta'$ (blue) biphasic regions, while the solid black lines denote the phase boundaries. The α region slightly expands ($0 < x < 0.18$) as temperature increases, leaving a narrow two-phase region of the $\alpha + \beta'$ region ($0.18 < x < 0.26$ at 1,000 K).

After introducing the vibrational contributions into the phase diagram construction, the phase diagram in Figure 2b comprises only 3 main phase regions, including the monophasic α and β regions and the $\alpha + \beta$ biphasic region. Moreover, as temperature increases, the $\alpha + \beta$ phase region shifts to higher values of niobium content ($0.74 < x < 0.82$), leaving a wide region of the α phase ($0 < x < 0.74$ at 1,000 K) but a narrower region of the β phase ($0.82 < x < 1$ at 1,000 K). This phase transition in Figure 2b, qualitatively agrees with the experimental findings (indicated by the colored points in Figure 2b).

Miao and Torardi conducted solid-state synthesis of $Li_3Nb_xTa_{1-x}O_4$ across the composition region at 1,273 K.[64] Their X-ray diffraction results indicated that $Li_3Nb_xTa_{1-x}O_4$ maintains an α-phase structure at $0 < x < 0.6$, $\alpha + \beta$ phases at

$0.6 < x < 0.8$, and β-phase at $0.8 < x < 1.0$, in a good agreement with our computational results. A comparable phase transition trend was also reported by Blasse,[65] revealing a greater dissolution ratio of Nb in α-Li_3TaO_4 than that of Ta in β-Li_3NbO_4 at synthesis temperature of 1,173 K.

Figure 3 emphasizes the thermodynamic properties of $Li_3Nb_xTa_{1-x}O_4$, where the colors represent the phase regions at different temperatures (α phase in orange, biphasic $\alpha + \beta$ region in blue, and β phase in green). The left panels describe the total Gibbs free energy of mixing, G_{mix} (blue points), and the configurational entropy of mixing, $S_{mix}(conf)$ (green points), computed at selected temperatures, 10, 50, 300, and 1,000 K. The right panels illustrate the vibrational entropy of mixing $S_{mix}(vib)$ as a function of composition (x) for the α-phase (orange) and β-phase (green). Star symbols denote the calculated $S_{mix}(vib)$ for the ground-state structures within each phase.

As shown in Figure 3a, the Gibbs free energy of mixing, $G_{mix} = E_{mix} - TS_{mix}$, decreases with increasing temperature due to configurational and vibrational entropy contributions. As x (i.e., the Nb concentration) increases from 0 to 1, $S_{mix}(conf)$ initially increases in α-phase region, reaching a maximum at $x = 0.5$ due to complete Nb/Ta disorder (for example, at 1,000 K), and then decreases in the β-phase region. The magnitudes of $S_{mix}(conf)$ values are comparable though in different phases. In Figure 3b, the vibrational entropies of mixing, $S_{mix}(vib)$, show a consistent increase with increasing Nb concentration in α- and β-phases. Notably, negative values of $S_{mix}(vib)$ are observed in the β-phase. Typically, in regimes of solid solution, negative values of vibrational entropy of mixing enhance thermal stability in ordered states, suppressing the formation of disordered structures at higher temperatures, leading to retrograde solubility.[66,67] This observation helps to explain the observed decrease in Ta solubility in the β-phase as temperature increases. Accounting for vibrational entropy differences (Figure 2b) between phases significantly corrects

transition temperatures relative to estimates based solely on configurational entropy (Figure 2a).

3.2. Li$^+$ Mobilities in Li$_3$Nb$_x$Ta$_{1−x}$O$_4$. Prior experimental studies on partially crystallized LiNb$_x$Ta$_{1−x}$O$_3$ reported enhanced Li-ion conductivities, exhibiting enhancements within 1 order of magnitude relative to the pure LiNbO$_3$ and LiTaO$_3$, contingent on composition and synthesis protocols.[29,31,32] Thus, we explore if Li-ion conductivity enhancements also manifest in the mixed Li$_3$Nb$_x$Ta$_{1−x}$O$_4$ system.

Point defects, including vacancies, interstitials, and antisite defects, as well as their concentrations, control Li-ion mobility in materials. Previous experimental characterizations and computational reports[18,24,27,68] suggested that LiMO$_3$ (M = Nb, and Ta) incorporates defects deviating from its stoichiometry. These point defects are characterized by ∼1% M$_{Li}$ antisites − where Li ions are replaced by Nb^{5+} or Ta^{5+} species − and ∼4% Li vacancies. Previously, Vyalikh et al. showed that Ta interstitials and Li vacancies are more likely to form in LiTaO$_3$.[69] Furthermore, the coexistence of LiMO$_3$ and Li$_3$MO$_4$ phases in the Li-M-O system is expected to favor defect formation within Li$_3$MO$_4$, leading to comparable defect concentrations between the two phases.

Stoichiometric Li$_3$TaO$_4$ and Li$_3$NbO$_4$ are poor ionic conductors due to their fully occupied Li sites.[70] While introducing defects, such as Li vacancies, is a known strategy to enhance conductivity,[27] the fundamental transport properties of these charge carriers are not well established.

To quantify the intrinsic Li-ion mobilities in these systems, we computationally investigate the low-vacancy limit (∼1%) regime of these Nb−Ta oxide alloys, which is described by introducing one Li vacancy per 32 formula units (Li$_{96}$Nb$_{32x}$Ta$_{32(1−x)}$O$_{128}$). Charge neutrality of the simulation was achieved by introducing a compensating background charge. Based on the phase diagram of Figure 2b, we selected configurations at various Nb concentrations (α-phase: x = 0, 0.125, and 0.1875; and β-phases: 0.6875, 0.75, and 1) from MC simulations at 300 K. The ionic conductivity of each structure was subsequently estimated by molecular dynamics using machine learned moment-tensor potentials (MTP-MD, see Section 2.5). The resulting conductivity, while modest, represents the intrinsic mobility in a dilute-defect scenario. However, it should be noted that the overall conductivity of a synthesized material is ultimately dictated by the total vacancy concentration generated by specific processing protocols. In practice, synthesis protocols are expected to generate a higher concentration of defects, leading to greater ionic conductivities than those predicted here.

The calculated Li-ion transport properties for the Li$_3$Nb$_x$Ta$_{1−x}$O$_4$ system reveal that cation mixing enhances ionic conductivity by lowering the activation energy for Li-ion migration. As shown in Figure 4, the migration barriers (E_a) decrease within both the Ta-rich α-phase (orange area) and the Nb-rich β-phase (green area) as they approach the central, phase-separated area.

Note, we did not calculate the ionic conductivities of structures in regimes of phase separation (x = 0.23−0.62, identified by the blue area in Figure 4). However, recent kinetic Monte Carlo simulations of solid electrolytes in either solid solution or phase separation regimes indicate that the overall ionic conductivities of many compositions are unaffected by the underlying phase behavior.[71]
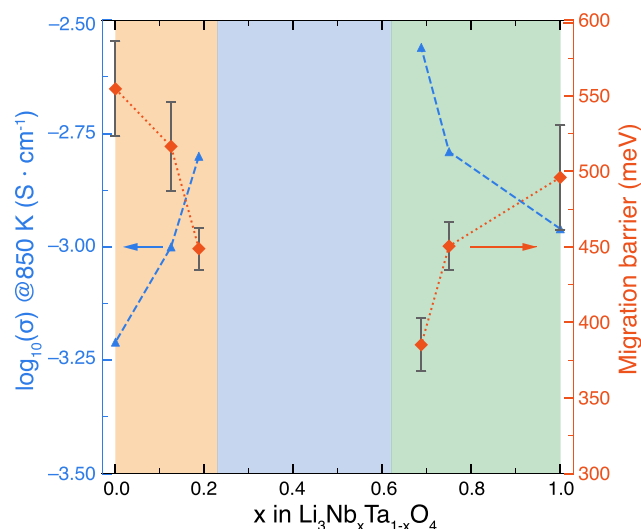
Figure 4. Temperature-dependent ionic conductivities σ (in S·cm^{-1}) (at 850 K) and Arrhenius-fitted migration barriers (in meV) of Li$_3$Nb$_x$Ta$_{1−x}$O$_4$ for x = 0, 0.125, 0.1875, 0.6875, 0.75, and 1 derived from machine learning MTP molecular dynamics calculations. Colored regions represent the phase distributions at 300 K: α phase, x = 0.00−0.23, $\alpha + \beta$ phases, x = 0.23−0.62, β phase, x = 0.62−1.00. The error bars of migration barriers fitted from the temperature-dependent Li$^+$ diffusivities are shown.

Specifically, in the α-phase, the average migration energy decreases from 555 ± 31 meV in pure Li$_3$TaO$_4$ (x = 0) to 449 ± 20 meV at an Nb concentration of x = 0.125. Conversely, in the β-phase, the barrier decreases from 496 ± 34 meV in pure Li$_3$NbO$_4$ (x = 1) to 385 ± 15 meV at x = 0.6875. This reduction in activation energy directly translates to higher Li-ion conductivities at elevated temperatures. At 850 K, the computed conductivity of the α-phase increases from 6.12 × 10^{-4} to 1.60 × 10^{-3} S·cm^{-1} as x increases from 0 to 0.1875. Similarly, in the β-phase, the Li-ion conductivities increase as more Ta is introduced, rising from 1.10 × 10^{-3} (x = 1) to 2.78 × 10^{-3} S·cm^{-1} (x = 0.6875).

Our calculated migration energy barriers for the stoichiometric end-members show good agreement with existing experimental data. For α-Li$_3$TaO$_4$, our computed migration barriers of 555 ± 31 meV (with 1% Li vacancies) match well with reported experimental values of ∼550 meV for Li-deficient samples (with ∼0.67% Li vacancies) and 630−680 meV for stoichiometric samples.[27,72] For β-Li$_3$NbO$_4$ (with 1% Li vacancies), the calculated migration barriers of ∼496 ± 34 meV are slightly lower than the experimentally observed values (580−850 meV) for crystalline and stoichiometric samples.[21,70,73]

Furthermore, the general trend of enhanced ionic transport upon mixing is consistent with findings in related material systems. For example, Yada et al. investigated partially crystallized Li−Nb−Ta oxides for battery interlayers and found that a mixed-cation composition (Li$_{56}$Nb$_{22}$Ta$_{22}$ oxide, x = 0.5) exhibited a higher ionic conductivity (4.2 × 10^{-6} S·cm^{-1}) than the end member compound LiNbO$_3$ (1.8 × 10^{-6} S·cm^{-1}). This supports our observation that blending Nb and Ta can be a beneficial strategy for improving Li-ion kinetics in these coating materials.

4. DISCUSSION

Niobium and tantalum oxides are widely used in applications demanding exceptional thermal stability and dielectric performance, including high-performance faradaic capacitors, high-temperature superalloys, nonlinear optics, and protective coatings.[36,74−76] Understanding the properties of functional oxide-based coating materials is also central to the development of high-energy density, safe rechargeable lithium-ion batteries with improved cycle stability and shelf life.

Although lithium-niobate-tantalate oxides have been implemented through trial-and-error procedures into commercial Li-ion batteries, there are just a handful of experimental investigations establishing a link between the improved battery figures of merit and the structure and transport properties of these oxides.[29,30,39] This work elucidates how mixing niobium and tantalum affects the phase behavior and connected properties of their respective lithium oxides.

Our previous investigation on Li−Nb−O and Li−Ta−O materials suggested that niobate and tantalate coatings feature as a mixture of different phases, $LiNbO_3$ and Li_3NbO_4, or $LiTaO_3$ and Li_3TaO_4, in various proportions.[24] The weight fractions of these phases (once coated on the active particles of positive electrode materials) are entirely controlled by the ratio of precursors and the calcination temperatures adopted during their preparation.[18,77]

Nonetheless, the correlation between the coexistence of Nb and Ta within a single coating matrix ($LiNb_xTa_{1−x}O_3$ and $Li_3Nb_xTa_{1−x}O_4$) and its thermodynamic characteristics and Li-ion transport behavior remains insufficiently investigated. We bridge this gap using advanced cluster-expansion-based Monte Carlo simulations that explicitly account for configurational and vibrational entropy, enabling a rigorous thermodynamic description of these complex oxides. Starting from thermodynamically meaningful structures of mixed $Li_3Nb_xTa_{1−x}O_4$, we have investigated the Li-ion transport characteristics in these oxides through state-of-the-art moment tensor machine learning potentials.

It is also crucial to consider the enhanced stability offered by the incorporation of Ta. Previous computational investigations have shown that $LiTaO_3$ and Li_3TaO_4 possess a wider stability window (vs Li/Li^+) than the mixture of $LiNbO_3$ and Li_3NbO_4, respectively.[78,79] In the comparison of $LiNbO_3$ and $LiTaO_3$ coatings by Lee and Park,[80] lithium tantalate coating materials appear superior in mitigating oxidative reactions between positive electrode materials and sulfide-based solid electrolytes. The improved mechanical properties are demonstrated by $LiTaO_3$ possessing higher bulk and Young's moduli than $LiNbO_3$.[81] $LiTaO_3$ has been shown to enhance the structural stability of positive electrode materials when coated on their particles.[82,83] These distinctions prompt the additional potential advantages of Nb/Ta mixing coating materials for enhanced performance.

4.1. Structural and Vibrational Origins of Nb and Ta Mixing Energetics.
Belonging to transition metals of the Group 5, Nb and Ta share similar electronic characteristics in their outer shells (Nb: $[Kr]$ $4d^45s^1$, Ta: $[Xe]$ $4f^{14}5d^36s^2$). The similarities between niobium and tantalum extend to their pentavalent cations, Nb^{5+} and Ta^{5+}, which, in 6-fold coordination, possess identical ionic radii of ∼0.64 Å.[33,84,85] Due to their identical charge and nearly identical ionic radii, Nb^{5+} and Ta^{5+} readily substitute for one another in a wide range of oxide and alloy systems—often referred to as

bronzes—without inducing appreciable lattice distortion. We utilize both qualitative and quantitative information for Nb^{5+} and Ta^{5+} to elucidate our findings in $Li_3Nb_xTa_{1−x}O_4$.

In general, a close inspection of the DFT-computed Nb/Ta orderings suggests shorter average Ta−O distances compared with Nb−O bond lengths (as shown in Figure S7, $LiNb_xTa_{1−x}O_3$, and Figure S8, $Li_3Nb_xTa_{1−x}O_4$ of the SI), in agreement with previous studies.[39,86−88] At first glance, these observations stand in marked contrast to Pearson's "hard and soft acids and bases theory",[89] as Ta^{5+} is considered a slightly softer cation than Nb^{5+} due to its greater polarizability and correspondingly lower charge density.

Unlike Li_3NbO_4 ($I\bar{4}3m$), a high-symmetry cubic analog phase for Li_3TaO_4 has never been reported, indicating that octahedral coordination is less favorable for Ta^{5+} within this structural framework.[65] Li_3NbO_4 features tetramers of Nb octahedron clusters, where each Nb^{5+} has three nearest neighbors Nb^{5+}s, with a high-density of pentavalent cations. In contrast, Ta^{5+} ions are more dispersed in Li_3TaO_4, which exhibits electrostatically stabilized zigzag chains of Ta octahedra, where each Ta^{5+} has only two Ta^{5+} nearest neighbors.

Consequently, the mixing of Ta into Li_3NbO_4 may introduce substantial lattice strain, necessitating "strong" atomic vibrational coupling with the Ta site centers to preserve the structure. Although the specific vibrational modes of $Li_3Nb_xTa_{1−x}O_4$ alloys are not explicitly investigated in this work, we observed a decrease in vibrational entropy of mixing with increasing Ta content (decreasing Nb amount) in the β-phase (Figure 3). As a result, Li_3NbO_4 is less likely to mix large amounts of Ta^{5+}, resulting in a progressively narrower region of β phase as the temperature increases (Figure 2b). On the contrary, the lower spatial density of Ta^{5+} in Li_3TaO_4 leads to weaker cation−cation interactions, facilitating mixing of Nb^{5+} to stabilize the α-phase.

Previously, Holder and collaborators have assumed that configurational entropy is a fixed function of composition.[40] Based on this argument, the same authors suggested that intersections of mixing enthalpy curves dictate the critical compositions defining miscibility gaps. From Figure 1b, the junction of the two tie lines occurs at approximately $x \sim 0.3$ (corresponding to $Li_3Nb_{0.3}Ta_{0.7}O_4$) − the onset of the miscibility gap. Upon introducing temperature-dependent vibrational contributions as in Figure 2, the width of the α-phase is significantly increased. Therefore, the critical point is shifted to much higher Nb concentrations, for example, $x \sim 0.75$ at 1,000 K. This result suggests that accounting explicitly for configurational and vibrational effects can significantly impact the phase behaviors of materials, in particular the miscibility of the heterostructural systems.

This set of evidence reinforces the idea that including vibrational entropy effects in addition to configurational entropy contributions (as usually done through cluster expansion and Monte Carlo approaches) appears crucial to reproduce the miscibility of Ta in Li_3NbO_4 (see Figure 2b). These findings underline the importance of incorporating vibrational entropy for accurate phase diagram predictions of complex materials,[67,90−92] especially when phases differ only subtly in configurational energy.

4.2. Li-Ion Mobility in $Li_3Nb_xTa_{1−x}O_4$.
Previously, we have shown that crystalline Li_3NbO_4 (and Li_3TaO_4) have higher Li-ion transport properties than crystalline $LiNbO_3$ (or $LiTaO_3$),[24] with the Li_3MO_4 phase fraction forming preferen-

tially with a rich defect landscape at higher calcination temperatures. Focusing on $Li_3Na_xTa_{1-x}O_4$ here, we have revealed that mixing Nb and Ta, i.e., substituting Ta with Nb in the α-phase (or replacing Nb with Ta in the β-phase) is a possible way to enhance Li-ion conductivities of these compounds.

The mechanism for the enhanced Li-ion conductivity upon mixing can be attributed to modifications of the energy landscape and local vibrational properties of the system. Introducing a guest cation creates localized strain and distorts the polyhedra that define the Li-ion diffusion pathways. In both α and β phases, partial substitution creates local site-energy heterogeneity that reduces the correlation between adjacent Li-ion hops, lowering the average activation barrier and opening percolating low-barrier pathways. Such behavior reflects a general mechanism reported for disordered oxides, where cation mixing disrupts long-range order and broadens the distribution of accessible Li sites.

In addition to static disorder imposed by Ta and Nb mixing during synthesis, vibrational effects might also modulate transport properties differently across the two phases. In the Ta-rich α-phase, the negative mixing vibrational free energy (Figure S11) suggests a stabilization of lattice softening upon Nb substitution, consistent with a reduction in bottleneck size that would further lower migration barriers. Conversely, in the Nb-rich β-phase, substituting with Ta yields a positive mixing vibrational free energy (Figure S11). This reveals that while this mixed state is vibrationally destabilized relative to the pure components, it might paradoxically promote faster ion migration. A more comprehensive understanding of ionic transport properties necessitates future investigations that precisely quantify the interplay between configurational and vibrational contributions, thereby elucidating the roles of structural disorder and lattice dynamics in complex materials.

5. CONCLUSION

In summary, we investigated the effect of niobium and tantalate mixing in lithium oxides, forming $Li_3Nb_xTa_{1-x}O_4$ alloys relevant to improving ionic conductivity and electrochemical performance in lithium-ion batteries. Using a multiscale approach parametrized on first-principles density functional theory calculations, we have successfully mapped the complex phase diagram of $Li_3Nb_xTa_{1-x}O_4$, demonstrating qualitative agreement with reported phase transitions.

Crucially, we unveiled the substantial influence of vibrational contributions on reducing the solubility of Ta in Li_3NbO_4. Moreover, our study highlights the potential for enhancing Li-ion transport performance in crystalline $Li_3Nb_xTa_{1-x}O_4$ through strategic Nb and Ta mixing. Such mixing exhibits similar effects on different phases, leading to an improvement in Li-ion conductivity in the β-phase and α-phase. These findings offer the potential to tailor ionic conductivities of $Li_3Nb_xTa_{1-x}O_4$ materials and optimize their performance as protective coatings in energy storage applications, high-performance faradaic capacitors, high-temperature superalloys, and nonlinear optics.

■ ASSOCIATED CONTENT

ⓢ Supporting Information

The Supporting Information is available free of charge at https://pubs.acs.org/doi/10.1021/acs.chemmater.5c02429.

Computational methodology and results of DFT calculations and Cluster Expansion fitting for both the $Li_3Nb_xTa_{1-x}O_4$ and $LiNb_xTa_{1-x}O_3$ systems; tabulated M-O bond lengths and free volume ratios for all DFT-calculated ordered structures; calculated phonon dispersion curves for the identified ground-state structures; a detailed description of the thermodynamic integration method employed in this work (PDF)

■ AUTHOR INFORMATION

Corresponding Author

Pieremanuele Canepa − *Department of Electrical and Computer Engineering, University of Houston, Houston, Texas 77204, United States; Texas Center of Superconductivity, University of Houston, Houston, Texas 77204, United States;* ⓞ orcid.org/0000-0002-5168-9253; Email: pcanepa@uh.edu

Authors

Hengning Chen − *Department of Materials Science and Engineering, National University of Singapore, Singapore 117575, Singapore;* ⓞ orcid.org/0009-0000-2475-4681

Zeyu Deng − *Department of Materials Science and Engineering, National University of Singapore, Singapore 117575, Singapore;* ⓞ orcid.org/0000-0003-0109-9367

Gopalakrishnan Sai Gautam − *Department of Materials Engineering, Indian Institute of Science, 560012 Bangalore, India;* ⓞ orcid.org/0000-0002-1303-0976

Yan Li − *Department of Materials Science and Engineering, National University of Singapore, Singapore 117575, Singapore*

Complete contact information is available at:
https://pubs.acs.org/10.1021/acs.chemmater.5c02429

Notes

The authors declare no competing financial interest.

■ REFERENCES

(1) Fernández-García, M.; Martínez-Arias, A.; Hanson, J. C.; Rodriguez, J. A. Nanostructured Oxides in Chemistry: Characterization and Properties. *Chem. Rev.* **2004**, *104*, 4063−4104.

(2) Dai, Z.; Pan, Z.; Wang, Z. Novel Nanostructures of Functional Oxides Synthesized by Thermal Evaporation. *Adv. Funct. Mater.* **2003**, *13*, 9−24.

(3) Yuan, C.; Wu, H. B.; Xie, Y.; Lou, X. W. D. Mixed Transition-Metal Oxides: Design, Synthesis, and Energy-Related Applications. *Angew. Chem., Int. Ed.* **2014**, *53*, 1488−1504.

(4) Culver, S. P.; Koerver, R.; Zeier, W. G.; Janek, J. On the Functionality of Coatings for Cathode Active Materials in Thiophosphate-Based All-Solid-State Batteries. *Adv. Energy Mater.* **2019**, *9*, No. 1900626.

(5) Tan, D. H. S.; Banerjee, A.; Chen, Z.; Meng, Y. S. From nanoscale interface characterization to sustainable energy storage using all-solid-state batteries. *Nat. Nanotechnol.* **2021**, *16*, 479.

(6) Li, C.; Zhang, H.; Fu, L.; Liu, H.; Wu, Y.; Rahm, E.; Holze, R.; Wu, H. Cathode materials modified by surface coating for lithium ion batteries. *Electrochim. Acta* **2006**, *51*, 3872−3883.

(7) Guan, P.; Zhou, L.; Yu, Z.; Sun, Y.; Liu, Y.; Wu, F.; Jiang, Y.; Chu, D. Recent progress of surface coating on cathode materials for high-performance lithium-ion batteries. *J. Energy Chem.* **2020**, *43*, 220−235.

(8) Janek, J.; Zeier, W. G. A solid future for battery development. *Nat. Energy* **2016**, *1*, 1−4.

(9) Goodenough, J. B.; Kim, Y. Challenges for Rechargeable Li Batteries. *Chem. Mater.* **2010**, *22*, 587−603.

(10) Liu, W.; Oh, P.; Liu, X.; Lee, M.; Cho, W.; Chae, S.; Kim, Y.; Cho, J. Nickel-Rich Layered Lithium Transition-Metal Oxide for High-Energy Lithium-Ion Batteries. *Angew. Chem., Int. Ed.* **2015**, *54*, 4440−4457.

(11) Wang, K.-X.; Li, X.-H.; Chen, J.-S. Surface and interface engineering of electrode materials for lithium-ion batteries. *Adv. Mater.* **2015**, *27*, 527−545.

(12) Xie, W.; Deng, Z.; Liu, Z.; Famprikis, T.; Butler, K. T.; Canepa, P. Effects of Grain Boundaries and Surfaces on Electronic and Mechanical Properties of Solid Electrolytes. *Adv. Energy Mater.* **2024**, *14*, No. 2304230.

(13) Meyerson, M. L.; Papa, P. E.; Heller, A.; Mullins, C. B. Recent Developments in Dendrite-Free Lithium-Metal Deposition through Tailoring of Micro- and Nanoscale Artificial Coatings. *ACS Nano* **2021**, *15*, 29−46.

(14) Kim, A.-Y.; Strauss, F.; Bartsch, T.; Teo, J. H.; Hatsukade, T.; Mazilkin, A.; Janek, J.; Hartmann, P.; Brezesinski, T. Stabilizing effect of a hybrid surface coating on a Ni-rich NCM cathode material in all-solid-state batteries. *Chem. Mater.* **2019**, *31*, 9664−9672.

(15) Famprikis, T.; Canepa, P.; Dawson, J. A.; Islam, M. S.; Masquelier, C. Fundamentals of inorganic solid-state electrolytes for batteries. *Nat. Mater.* **2019**, *18*, 1278−1291.

(16) Kato, Y.; Hori, S.; Saito, T.; Suzuki, K.; Hirayama, M.; Mitsui, A.; Yonemura, M.; Iba, H.; Kanno, R. High-power all-solid-state batteries using sulfide superionic conductors. *Nat. Energy* **2016**, *1*, 1−7.

(17) Ohta, N.; Takada, K.; Sakaguchi, I.; Zhang, L.; Ma, R.; Fukuda, K.; Osada, M.; Sasaki, T. LiNbO₃-coated LiCoO₂ as cathode material for all solid-state lithium secondary batteries. *Electrochem. Commun.* **2007**, *9*, 1486−1490.

(18) Xin, F.; Zhou, H.; Zong, Y.; Zuba, M.; Chen, Y.; Chernova, N. A.; Bai, J.; Pei, B.; Goel, A.; Rana, J.; Wang, F.; An, K.; Piper, L. F. J.; Zhou, G.; Whittingham, M. S. What is the Role of Nb in Nickel-Rich Layered Oxide Cathodes for Lithium-Ion Batteries? *ACS Energy Lett.* **2021**, *6*, 1377−1382.

(19) Li, T.; Chang, X.; Xin, Y.; Liu, Y.; Tian, H. Synergistic Strategy Using Doping and Polymeric Coating Enables High-Performance High-Nickel Layered Cathodes for Lithium-Ion Batteries. *J. Phys. Chem. C* **2023**, *127*, 8448−8461.

(20) You, M. J.; Jung, J.; Byeon, Y. S.; Jung, J. Y.; Hong, Y.; Park, M.-S. Controlled crystallinity of LiTaO₃ surface layer for single-crystalline Ni-rich cathodes for lithium-ion batteries and all-solid-state batteries. *Chem. Eng. J.* **2024**, *483*, No. 149199.

(21) Glass, A. M.; Nassau, K.; Negran, T. J. Ionic conductivity of quenched alkali niobate and tantalate glasses. *J. Appl. Phys.* **1978**, *49*, 4808−4811.

(22) Uhlendorf, J.; Ruprecht, B.; Witt, E.; Chandran, C. V.; Dörrer, L.; Hüger, E.; Strauß, F.; Heitjans, P.; Schmidt, H. Slow Lithium Transport in Metal Oxides on the Nanoscale. *Z. Phys. Chem.* **2017**, *231*, 1423−1442.

(23) Hüger, E.; Riedel, L.; Zhu, J.; Stahn, J.; Heitjans, P.; Schmidt, H. Lithium Niobate for Fast Cycling in Li-ion Batteries: Review and New Experimental Results. *Batteries* **2023**, *9*, No. 244.

(24) Chen, H.; Deng, Z.; Li, Y.; Canepa, P. On the Active Components in Crystalline Li-Nb-O and Li-Ta-O Coatings from First Principles. *Chem. Mater.* **2023**, *35*, 5657−5670.

(25) Nyman, M.; Anderson, T. M.; Provencio, P. P. Comparison of Aqueous and Non-aqueous Soft-Chemical Syntheses of Lithium Niobate and Lithium Tantalate Powders. *Cryst. Growth Des.* **2009**, *9*, 1036−1040.

(26) Lu, G.; Peng, W.; Zhang, Y.; Wang, X.; Shi, X.; Song, D.; Zhang, H.; Zhang, L. Study on the formation, development and coating mechanism of new phases on interface in LiNbO₃-coated LiCoO₂. *Electrochim. Acta* **2021**, *368*, No. 137639.

(27) Kim, C.; Kim, Y.-I. Ionic conductivity of Li₃TaO₄ depending on polymorphism and non-stoichiometric defects. *Ceram. Int.* **2023**, *49*, 29237−29244.

(28) Liao, Y.; Singh, P.; Li, W.; Goodenough, J. B. Comparison of Li⁺ conductivity in Li₃₋ₓNb₁₋ₓMₓO₄ (M = W, Mo) with that in Li₃₋₂ₓNiₓNbO₄. *Mater. Res. Bull.* **2013**, *48*, 1372−1375.

(29) Yada, C.; Lee, C. E.; Laughman, D.; Hannah, L.; Iba, H.; Hayden, B. E. A High-Throughput Approach Developing Lithium-Niobium-Tantalum Oxides as Electrolyte/Cathode Interlayers for High-Voltage All-Solid-State Lithium Batteries. *J. Electrochem. Soc.* **2015**, *162*, A722−A726.

(30) Zhang, W.; Weber, D. A.; Weigand, H.; Arlt, T.; Manke, I.; Schröder, D.; Koerver, R.; Leichtweiss, T.; Hartmann, P.; Zeier, W. G.; Janek, J. Interfacial Processes and Influence of Composite Cathode Microstructure Controlling the Performance of All-Solid-State Lithium Batteries. *ACS Appl. Mater. Interfaces.* **2017**, *9*, 17835−17845.

(31) Liu, Y.; Wang, C.; Yoon, S. G.; Han, S. Y.; Lewis, J. A.; Prakash, D.; Klein, E. J.; Chen, T.; Kang, D. H.; Majumdar, D.; Gopalaswamy, R.; McDowell, M. T. Aluminum foil negative electrodes with multiphase microstructure for all-solid-state Li-ion batteries. *Nat. Commun.* **2023**, *14*, No. 3975.

(32) Wang, C.; Liang, J.; Hwang, S.; et al. Unveiling the critical role of interfacial ionic conductivity in all-solid-state lithium batteries. *Nano Energy* **2020**, *72*, 104686.

(33) Shannon, R. D. Revised effective ionic radii and systematic studies of interatomic distances in halides and chalcogenides. *Acta Crystallogr. A* **1976**, *32*, 751−767.

(34) Bartasyte, A.; Glazer, A.; Wondre, F.; Prabhakaran, D.; Thomas, P.; Huband, S.; Keeble, D.; Margueron, S. Growth of LiNb₁₋ₓTaₓO₃ solid solution crystals. *Mater. Chem. Phys.* **2012**, *134*, 728−735.

(35) Shimura, F.; Fujino, Y. Crystal growth and fundamental properties of LiNb₁₋ᵧTaᵧO₃. *J. Cryst. Growth* **1977**, *38*, 293−302.

(36) Huband, S.; Keeble, D. S.; Zhang, N.; Glazer, A. M.; Bartasyte, A.; Thomas, P. A. Crystallographic and optical study of LiNb₁₋ₓTaₓO₃. *Acta Crystallogr. B* **2017**, *73*, 498−506.

(37) Suhak, Y.; Roshchupkin, D.; Redkin, B.; Kabir, A.; Jerliu, B.; Ganschow, S.; Fritze, H. Correlation of Electrical Properties and Acoustic Loss in Single Crystalline Lithium Niobate-Tantalate Solid Solutions at Elevated Temperatures. *Crystals* **2021**, *11*, No. 398.

(38) Roshchupkin, D.; Emelin, E.; Plotitcyna, O.; et al. Single crystals of ferroelectric lithium niobate-tantalate LiNb₁₋ₓTaₓO₃ solid solutions for high-temperature sensor and actuator applications. *Acta Crystallogr. B* **2020**, *76*, 1071−1076.

(39) Rüsing, M.; Sanna, S.; Neufeld, S.; Berth, G.; Schmidt, W. G.; Zrenner, A.; Yu, H.; Wang, Y.; Zhang, H. Vibrational properties of LiNb₁₋ₓTaₓO₃ mixed crystal. *Phys. Rev. B* **2016**, *93*, No. 184305.

(40) Holder, A. M.; Siol, S.; Ndione, P. F.; et al. Novel phase diagram behavior and materials design in heterostructural semiconductor alloys. *Sci. Adv.* **2017**, *3*, No. 1700270.

(41) Cordell, J. J.; Pan, J.; Tamboli, A. C.; Tucker, G. J.; Lany, S. Probing configurational disorder in ZnGeN₂ using cluster-based Monte Carlo. *Phys. Rev. Mater.* **2021**, *5*, No. 024604.

(42) Brooks, C.; Lany, S. Heterostructural alloy phase diagram for (Cd₁₋ₓZnₓ)₃As₂. *Phys. Rev. Mater.* **2024**, *8*, No. L061201.

(43) Kresse, G.; Furthmüller, J. Efficient iterative schemes forab initiototal-energy calculations using a plane-wave basis set. *Phys. Rev. B* **1996**, *54*, 11169−11186.

(44) Furness, J. W.; Kaplan, A. D.; Ning, J.; Perdew, J. P.; Sun, J. Accurate and Numerically Efficient r²SCAN Meta-Generalized Gradient Approximation. *J. Phys. Chem. Lett.* **2020**, *11*, 8208−8215.

(45) Ewald, P. P. Die Berechnung optischer und elektrostatischer Gitterpotentiale. *Ann. Phys.* **1921**, *369*, 253−287.

(46) Ong, S. P.; Richards, W. D.; Jain, A.; Hautier, G.; Kocher, M.; Cholia, S.; Gunter, D.; Chevrier, V. L.; Persson, K. A.; Ceder, G. Python Materials Genomics (pymatgen): A robust, open-source python library for materials analysis. *Comput. Mater. Sci.* **2013**, *68*, 314−319.

(47) Sanchez, J.; Ducastelle, F.; Gratias, D. Generalized cluster description of multicomponent systems. *Physica A* **1984**, *128*, 334−350.

(48) CASM Developers CASMcode: v0.2.1 (visited on 2024/03/24). 2017.

(49) Puchala, B.; der Ven, A. V. Thermodynamics of the Zr-O system from first-principles calculations. *Phys. Rev. B* **2013**, *88*, No. 094108.

(50) Puchala, B.; Thomas, J. C.; Natarajan, A. R.; Goiri, J. G.; Behara, S. S.; Kaufman, J. L.; Van der Ven, A. CASM — A software package for first-principles based study of multicomponent crystalline solids. *Comput. Mater. Sci.* **2023**, *217*, No. 111897.

(51) Nelson, L. J.; Hart, G. L. W.; Zhou, F.; Ozoliņš, V. Compressive sensing as a paradigm for building physics models. *Phys. Rev. B* **2013**, *87*, No. 035125.

(52) Togo, A.; Tanaka, I. First principles phonon calculations in materials science. *Scripta Mater.* **2015**, *108*, 1−5.

(53) Hinuma, Y.; Pizzi, G.; Kumagai, Y.; Oba, F.; Tanaka, I. Band structure diagram paths based on crystallography. *Comput. Mater. Sci.* **2017**, *128*, 140−184.

(54) Gan, C. K.; Feng, Y. P.; Srolovitz, D. J. First-principles calculation of the thermodynamics of $In_xGa_{1−x}N$ alloys: Effect of lattice vibrations. *Phys. Rev. B* **2006**, *73*, No. 235214.

(55) Chen, H.; Deng, Z.; Gautam, G. S.; Li, Y.; Canepa, P. CASMcode for vibration 2025 https://github.com/caneparesearch/CASMcode/tree/hengning_Fvib (visited March 30, 2025).

(56) van de Walle, A.; Asta, M. Self-driven lattice-model Monte Carlo simulations of alloy thermodynamic properties and phase diagrams. *Model. Simul. Mater. Sc.* **2002**, *10*, 521−538.

(57) Kim, C.; Pham, T. L.; Lee, J.-S.; Kim, Y.-I. Synthesis, thermal analysis, and band gap of ordered and disordered complex rock salt Li_3TaO_4. *J. Solid State Chem.* **2022**, *315*, No. 123450.

(58) Hsiao, Y.-J.; Fang, T.-H.; Lin, S.-J.; Shieh, J.-M.; Ji, L.-W. Preparation and luminescent characteristic of Li_3NbO_4 nanophosphor. *J. Lumin.* **2010**, *130*, 1863−1865.

(59) van de Walle, A.; Ceder, G. The effect of lattice vibrations on substitutional alloy thermodynamics. *Rev. Mod. Phys.* **2002**, *74*, 11−45.

(60) Wolverton, C.; Ozolins, V.; Zunger, A. Short-range-order types in binary alloys: a reflection of coherent phase stability. *J. Phys.:Condens. Matter* **2000**, *12*, 2749−2768.

(61) Shchyglo, O.; Díaz-Ortiz, A.; Udyansky, A.; Bugaev, V. N.; Reichert, H.; Dosch, H.; Drautz, R. Theory of size mismatched alloy systems: many-body Kanzaki forces. *J. Phys.:Condens. Matter* **2008**, *20*, No. 045207.

(62) Zhuravlev, I. A.; Barabash, S. V.; An, J. M.; Belashchenko, K. D. Phase stability, ordering tendencies, and magnetism in single-phase fcc Au-Fe nanoalloys. *Phys. Rev. B* **2017**, *96*, No. 134109.

(63) Zhuravlev, I. A.; An, J. M.; Belashchenko, K. D. Microscopic first-principles model of strain-induced interaction in concentrated size-mismatched alloys. *Phys. Rev. B* **2014**, *90*, No. 214108.

(64) Miao, C.; Torardi, C. X-Ray and Ultraviolet Luminescence of $Li_3Ta_{1−x}Nb_xO_4$ Prepared by Flux Synthesis and Characterization of a New High Efficiency X-Ray Phosphor. *J. Solid State Chem.* **1999**, *145*, 110−115.

(65) Blasse, G. The ternary system $Li_3(Nb,Sb,Ta)O_4$. *J. Inorg. Nucl. Chem.* **1965**, *27*, 2117−2119.

(66) Benz, R. Entropies of mixing of solids with a retrograde solidus. *J. Phys. Chem. Solids* **1970**, *31*, 713−727.

(67) Delaire, O.; Swan-Wood, T.; Fultz, B. Negative Entropy of Mixing for Vanadium-Platinum Solutions. *Phys. Rev. Lett.* **2004**, *93*, No. 185704.

(68) Iyi, N.; Kitamura, K.; Izumi, F.; Yamamoto, J.; Hayashi, T.; Asano, H.; Kimura, S. Comparative study of defect structures in lithium niobate with different compositions. *J. Solid State Chem.* **1992**, *101*, 340−352.

(69) Vyalikh, A.; Zschornak, M.; Köhler, T.; Nentwich, M.; Weigel, T.; Hanzig, J.; Zaripov, R.; Vavilova, E.; Gemming, S.; Brendler, E.; Meyer, D. C. Analysis of the defect clusters in congruent lithium tantalate. *Phys. Rev. Mater.* **2018**, *2*, No. 013804.

(70) Ruprecht, B.; Heitjans, P. Ultraslow lithium diffusion in Li_3NbO_4 probed by ^7Li stimulated echo NMR spectroscopy. *Diffus. Fundam.* **2010**, *12*, 100−101.

(71) Deng, Z.; Mishra, T. P.; Mahayoni, E.; Ma, Q.; Tieu, A. J. K.; Guillon, O.; Chotard, J.-N.; Seznec, V.; Cheetham, A. K.; Masquelier, C.; Gautam, G. S.; Canepa, P. Fundamental investigations on the sodium-ion transport properties of mixed polyanion solid-state battery electrolytes. *Nat. Commun.* **2022**, *13*, No. 4470.

(72) Shari, S.; Tan, K.; Khaw, C.; Zainal, Z.; Lee, O.; Chen, S. Subsolidus solution and ionic conductivity of rock-salt structured $Li_{3+5x}Ta_{1−x}O_4$ electroceramics. *Mater. Sci.-Pol.* **2020**, *38*, 465−474.

(73) de Azevêdo, M. R.; Oliveira, M.; Wendy, L.; Vaz, J.; Almeida, R. M.; Viana, B. C.; Tanaka, A. A.; de Menezes, A. S.; Mouta, R.; dos Santos, C. C. Thermal expansion and electrical conductivity of the battery material Li_3NbO_4 in the cation-ordered rocksalt phase. *J. Alloys Compd.* **2025**, *1016*, No. 178786.

(74) Bartasyte, A.; Margueron, S.; Glazer, A. M.; Simon, E.; Gregora, I.; Huband, S.; Thomas, P. A. Vibrational modes and overlap matrix of $LiNb_{1−x}Ta_xO_3$ mixed crystals. *Phys. Rev. B* **2019**, *99*, No. 094306.

(75) Bernhardt, F.; Pfeiffer, F. A.; Schug, F.; Sanna, S.; Pfannstiel, A.; Hehemann, T.; Imlau, M.; Ganschow, S. Ground- and excited-state properties of $LiNb_{1−x}Ta_xO_3$ solid solutions. *Phys. Rev. Mater.* **2024**, *8*, No. 054403.

(76) Kofahl, C.; Ganschow, S.; Bernhardt, F.; El Azzouzi, F.; Sanna, S.; Fritze, H.; Schmidt, H. Li-diffusion in lithium niobate - tantalate solid solutions. *Solid State Ionics* **2024**, *409*, No. 116514.

(77) Zhang, Y.; Zhou, E.; Song, D.; Shi, X.; Wang, X.; Guo, J.; Zhang, L. Effects on electrochemical performances for host material caused by structure change of modifying material. *Phys. Chem. Chem. Phys.* **2014**, *16*, 17792.

(78) Xiao, Y.; Miara, L. J.; Wang, Y.; Ceder, G. Computational Screening of Cathode Coatings for Solid-State Batteries. *Joule* **2019**, *3*, 1252−1275.

(79) Zhu, Y.; He, X.; Mo, Y. First principles study on electrochemical and chemical stability of solid electrolyte-electrode interfaces in all-solid-state Li-ion batteries. *J. Mater. Chem. A* **2016**, *4*, 3253−3266.

(80) Lee, J. S.; Park, Y. J. Comparison of $LiTaO_3$ and $LiNbO_3$ Surface Layers Prepared by Post- and Precursor-Based Coating Methods for Ni-Rich Cathodes of All-Solid-State Batteries. *ACS Appl. Mater. Interfaces.* **2021**, *13*, 38333−38345.

(81) Wang, Y.; Ye, L.; Fitzhugh, W.; Chen, X.; Li, X. Interface Coating Design for Dynamic Voltage Stability of Solid-State Batteries. *Adv. Energy Mater.* **2023**, *13*, No. 2302288.

(82) Gaillac, R.; Pullumbi, P.; Coudert, F.-X. ELATE: an open-source online application for analysis and visualization of elastic tensors. *J. Phys.:Condens. Matter* **2016**, *28*, No. 275201.

(83) Lee, H. B.; Hoang, T. D.; Byeon, Y. S.; Jung, H.; Moon, J.; Park, M.-S. Surface Stabilization of Ni-Rich Layered Cathode Materials via Surface Engineering with $LiTaO_3$ for Lithium-Ion Batteries. *ACS Appl. Mater. Interfaces.* **2022**, *14*, 2731−2741.

(84) Shannon, R. D.; Prewitt, C. T. Effective ionic radii in oxides and fluorides. *Acta Crystallogr. B* **1969**, *25*, 925−946.

(85) *Fundamentals of crystallography*, 3rd ed.; Giacovazzo, C., Ed.; IUCr Texts on crystallography 15; Oxford University Press: Oxford, UK, 2012.

(86) du Boulay, D.; Sakaguchi, A.; Suda, K.; Ishizawa, N. Reinvestigation of β-Li_3TaO_4. *Acta Crystallogr. E* **2003**, *59*, i80−i82.

(87) Jacquet, Q.; Perez, A.; Batuk, D.; Van Tendeloo, G.; Rousse, G.; Tarascon, J.-M. The $Li_3Ru_yNb_{1−y}O_4$ $(0 ≤ y ≤ 1)$ System: Structural Diversity and Li Insertion and Extraction Capabilities. *Chem. Mater.* **2017**, *29*, 5331−5343.

(88) Radhakrishnan, A. N.; Rao, P. P.; Mahesh, S. K.; Thampi, D. S. V.; Koshy, P. Role of Bond Strength on the Lattice Thermal Expansion and Oxide Ion Conductivity in Quaternary Pyrochlore Solid Solutions. *Inorg. Chem.* **2012**, *51*, 2409−2419.

(89) Pearson, R. G. Hard and Soft Acids and Bases. *J. Am. Chem. Soc.* **1963**, *85*, 3533−3539.

(90) Neuhaus, J.; Leitner, M.; Nicolaus, K.; Petry, W.; Hennion, B.; Hiess, A. Role of vibrational entropy in the stabilization of the high-temperature phases of iron. *Phys. Rev. B* **2014**, *89*, No. 184302.

(91) Shao, W.; Guevara-Vela, J. M.; Fernández-Caballero, A.; Liu, S.; LLorca, J. Accurate prediction of the solid-state region of the Ni-Al phase diagram including configurational and vibrational entropy and magnetic effects. *Acta Mater.* **2023**, *253*, No. 118962.

(92) Ozoliņš, V.; Wolverton, C.; Zunger, A. First-principles theory of vibrational effects on the phase stability of Cu-Au compounds and alloys. *Phys. Rev. B* **1998**, *58*, R5897−R5900.